We are IntechOpen, the world's leading publisher of Open Access books Built by scientists, for scientists

6,900
Open access books available

186,000
International authors and editors

200M
Downloads

154
Countries delivered to

Our authors are among the

TOP 1%
most cited scientists

12.2%
Contributors from top 500 universities

CLARIVATE ANALYTICS
BOOK CITATION INDEX
INDEXED

WEB OF SCIENCE™

Selection of our books indexed in the Book Citation Index
in Web of Science™ Core Collection (BKCI)

Interested in publishing with us?
Contact book.department@intechopen.com

Numbers displayed above are based on latest data collected.
For more information visit www.intechopen.com

Imaging Methods of Concrete Structure Based on Impact-Echo Test

Pei-Ling Liu and Po-Liang Yeh

National Taiwan University, Institute of Applied Mechanics
Taiwan

1. Introduction

The impact echo method is a non-destructive test of concrete structures. This method was developed in 1980s (Sansalone & Carino, 1986) and nowadays is extensively used because of its simplicity and robustness. In the impact echo test, an impact force is applied on the surface of the target structure. Then, a transducer is used to measure to response of the structure. Transforming the time signal to the frequency domain, one can determine the depth of the reflector beneath the test point.

The impact echo test is a point–wise detection method. The non-destructive examination of a structure usually requires a large amount of tests. How to integrate the test results to get an overall picture about the condition of the structure is a challenging task. In order to simplify the interpretation, many imaging methods were proposed, providing direct information on the concrete interior.

This chapter introduces several imaging methods based on the impact echo test, including spectral B- and C-scan, spectral tomography, surface rendering, and volume rendering. These imaging methods can be used to determine the size and location of internal defects in concrete structures. Several numerical and experimental examples are given to illustrate the results of these imaging methods. The features of these methods are also compared.

2. The impact echo test and depth spectrum

2.1 Impact echo test

In the impact echo test, a steel ball or a hammer is used to produce a wave source on the surface of the structure. Consequently, stress waves are generated and propagate in the structure. A transducer is placed near the impact point to measure the response of the structure. Then, the received signals are recorded for data analysis.

If there is an interface beneath the test point, the longitudinal waves generated by the impact will bounce between the top surface and the interface. Such echo waves will form a peak in the spectrum of the signal. The peak frequency f and the depth of the interface d is related by the following formula (Sansalone & Carino, 1986):

$$d = C_p / 2f \tag{1}$$

where C_p is the velocity of the longitudinal wave. Equation 1 is valid only when the acoustic impedance of the material on the other side of the interface is less than that of concrete. If the material is stiffer, e.g., steel, the factor 2 in Eq. 1 should be replaced by 4.

It is proposed in the literature (Gibson & Popovics, 2005; Lin & Sansalone, 1992; Sansalone & Streett, 1997; Schubert & Köhler, 2008; Zhu & Popovics, 2007) that the depth obtained by Eq. 1 be multiplied by a correction factor to eliminate the discrepancy between the actual and predicted depths. The correction factor is dependent on the geometry of the structure. Its value has been determined for a few types of structural members. When imaging method is adopted to examine structures with defects, the geometry of the target structure is complex. It is almost impossible to choose an appropriate value for correction factor. Hence, Eq. 1 is used directly in the imaging process.

The Fourier analysis is the most widely used approach to construct the spectrum of the test response. However, the Fourier spectra usually contain ripples and multiple peaks generated by the transform process. Such artificial interferences may jeopardize the interpretation of test results (Yeh & Liu, 2008). Several time–frequency techniques have been proposed in the literature to prevent the interferences, for example, the wavelet transform and the Hilbert–Huang transform (Abraham et al., 2000; Algernon & Wiggenhauser, 2005; Lin et al., 2009; Shokouhi et al., 2006; Yeh & Liu, 2008). However, there is a trade-off because none of these methods would produce echo peaks as sharp as the Fourier transform does.

2.2 Depth spectrum

No matter which transform is adopted, the horizontal axis of the spectrum is the frequency, not depth. For the imaging purpose, it is preferable to have depth as the horizontal axis. The horizontal axis of the spectrum can be easily transformed to the depth axis by applying Eq. 1, as proposed by Yeh and Liu (2009). The frequency-depth transformation procedure is as follows:

Suppose $a(f)$ is the original spectrum of a signal.

1. Select an appropriate depth interval Δz.
2. Apply Eq. 1 to $i\Delta z$, $i = 1, 2, ...$ to find the corresponding frequency f_i.
3. Determine the maximum amplitude $\hat{a}_i$ in each interval (f_i, f_{i-1}), $i = 1, 2, ...$, as shown in Fig. 1.
4. Plotting $\hat{a}_i$ versus $i\Delta z$ yields the depth spectrum of the signal.

Notice that $\hat{a}_i$, instead of $a(f_i)$, is used to plot the depth spectrum. This is to insure that no peak is left out in the depth spectrum since peaks are the most important information in the spectrum. One should also know that the transformation cannot start from $z=0$ because it maps to $f = \infty$.

The depth spectrum constructed as above has a constant depth interval, which is convenient for image processing. However, the data points in the Fourier spectrum are not totally retained. Therefore, some of the details in the Fourier spectrum are not reproduced in the depth spectrum. The peaks, which contain the most important information, are preserved,

but they may not appear at the precise depth. The maximal depth deviation of a peak is $\Delta z/2$. Therefore, it is advisable to make the depth interval as short as possible.
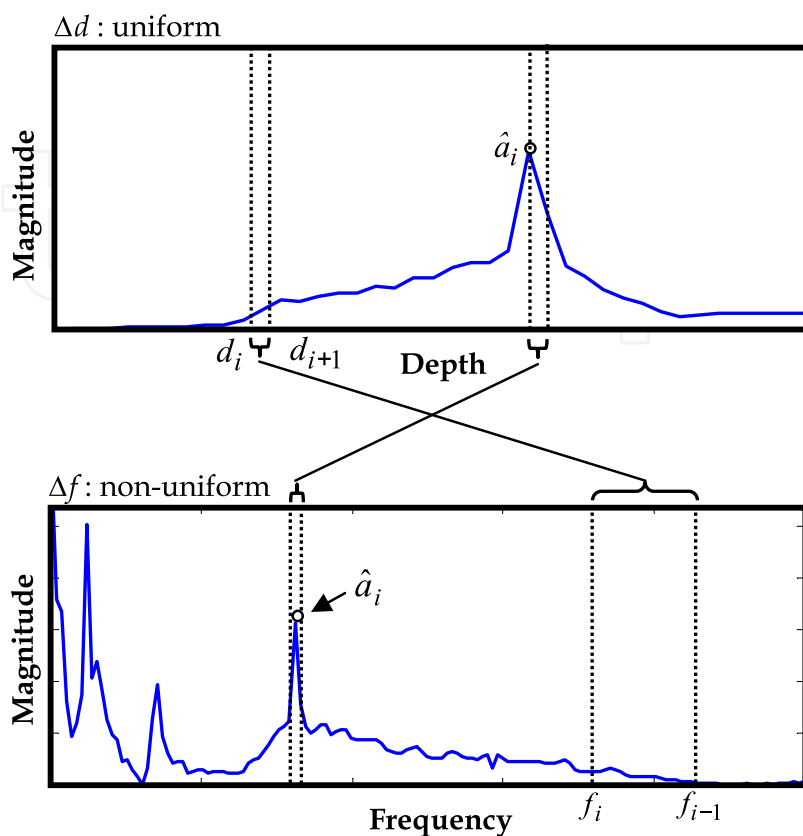

Fig. 1. Frequency-depth transformation

The depth spectrum is useful for the imaging of impact echo data. It has another advantage if the depth D of the concrete structure is known. In the impact echo test, several vibration modes of the structure will be induced. The impact echo is one of them. Unfortunately, the peaks caused by the lower–modes are often higher than the echo peak in the spectrum. This complicates the interpretation of results. The frequencies of the lower modes usually correspond to depths greater than D. Hence, if the depth spectrum is drawn only for the depth range $0 \leq z \leq D$, the lower–mode peaks do not appear. That simplifies the image interpretation.

3. Imaging methods

In general, the imaging of impact echo data contains three steps: data acquisition, data construction, and image rendering. The details of these steps will be introduced in the following sections.

3.1 Data acquisition and construction

To acquire data for image rendering, one has to conduct a series of impact echo tests on the target structure. Firstly, select a coordinate system such that the x-y plane coincides with surface of the concrete. Secondly, draw a mesh on the concrete surface, and perform the

impact echo test at each grid of the mesh, as shown in Fig. 2(a). The location of the impact and receiver can be chosen arbitrarily inside the grid. However, their midpoint should be located at the center of a grid.

Then, apply the Fourier transform or other transforms to the test signals to obtain the frequency spectra. In tomography and 3D imaging, the spectra are further transformed into the depth spectra.

After obtaining the spectra, one can proceed with the construction of data. Assume that the numbers of test points along the x and y directions are n_x and n_y, respectively, and each spectrum contains n_z data points. All the spectra are assembled into an $n_x \times n_y \times n_z$ matrix, $V[i,j,k]$. The array $V[i,j,1 \leq k \leq n_z]$ is simply the amplitude of spectrum under test point (i, j).

After the volume data is constructed, one may apply any of the imaging methods to depict the interior of concrete structure.

Notice that in tomography and 3D imaging, each vector $V[i,j,1 \leq k \leq n_z]$ is a depth spectrum. Suppose the grid size of the test mesh is $\Delta x \times \Delta y$ and the depth interval of the depth spectrum is Δz, each element in $V[i,j,k]$ corresponds to a voxel (volume element) in the space with voxel size $\Delta x \times \Delta y \times \Delta z$. Hence, the matrix maps to a rectangular solid with side lengths L_x, L_y, and L_z, where $L_x = n_x \Delta x$, $L_y = n_y \Delta y$, and $L_z = n_z \Delta z$. In this case, $V[i,j,k]$ represents the reflection energy from voxel $[i,j,k]$ in the rectangular solid.

In spectral B- or C-scan, on the other hand, each vector $V[i,j,1 \leq k \leq n_z]$ is a frequency spectrum. Hence, the third axis is frequency, not depth. Therefore, the matrix does not map to a rectangular solid in the space.

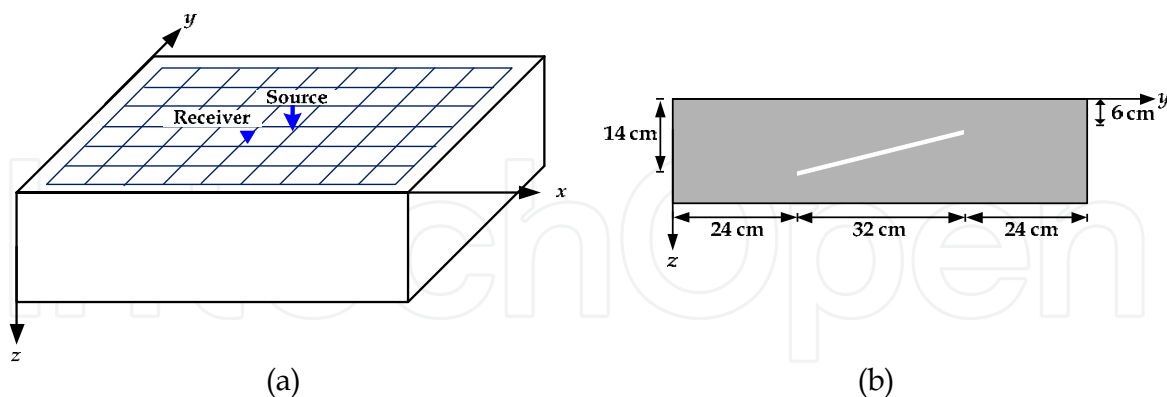(a)   (b)

Fig. 2. (a) Test mesh on the concrete surface and (b) side view of the example specimen

In this chapter, both numerical simulations and model tests are presented to illustrate the imaging methods. A concrete specimen with an slant internal crack is considered. The dimension of the specimen is 80 cm (L) × 80 cm (W) × 20 cm (H). The depth of the internal crack ranges from 6 cm to 14 cm beneath the surface, as shown in Fig. 2(b). The coordinates of the four corners of the crack are [x, y, z] = [24, 24, 14], [24, 56, 14], [56, 24, 6], and [56, 56, 6] (in cm).

The test mesh on the specimen is a 76 cm × 76 cm square with 19 × 19 grids, leaving 2 cm of margins on the four sides. In each test, the impact source and the receiver were located at the upper right and lower left corners of a grid, respectively.

In the numerical simulation, the finite element code LS–Dyna970 (Hallquist, 2003) was adopted to simulate the response of the concrete specimen due to the impact of a steel ball. Three–dimensional solid elements with side length 1cm were used in the numerical simulation. The mass density, Young's modulus, Poisson's ratio, and the longitudinal wave speed of the concrete are 2300 kg/m³, 33.1 GPa, 0.2, and 4000 m/s, respectively.

A time–varying pressure was applied to the surface to simulate the impact of a steel ball with a diameter of 6 mm. According to Goldsmith (1960), the pressure was approximated by a half–sine function with a contact time t_c= 25 µs. The total time of simulation was 3 ms, and the time increment was 3 msec/1024 = 2.93 µs.

Non–reflecting boundary conditions were applied on the four sides of the blocks to prevent waves reflecting from the boundaries. As such, the examples could focus on the results of imaging methods, excluding the effect of specimen geometry.

In the model test, the dimension of the concrete specimen and the crack location are identical to those of the numerical model. The longitudinal wave velocity of the concrete is 3890 m/s. In the experiment, a steel ball with diameter 6 mm was dropped on the concrete surface to produce the impact source. A conical transducer, developed at the Institute of Applied Mechanics, National Taiwan University, was adopted to measure the vertical displacement on the concrete surface. The impact and receiver locations were the same as in the numerical examples. The received voltage signals were enhanced by an amplifier and then recorded by a digital oscilloscope (LeCroy WavePro940). In the model tests, the sampling rate was 1 MHz, and the total sampling time was 5 msec.

Unlike the numerical tests, the energy of the impact source in the model tests may vary from test to test. Therefore, the experimental data were normalized based on the amplitude of the surface wave.

3.2 Spectral B-scan and C-scan

The spectral B– and C–scan methods were firstly proposed by Liu and Yiu (2002) to detect the internal cracks in concrete. The spectral B–scan was adopted by Schubert et al. (2004) to measure the thickness of concrete specimens. Kohl et al. (2005) further extended the idea so that one could combine impact echo data with ultrasonic data to construct B– and C–scan images.

The concepts of spectral B- and C-scans are similar to the ultrasonic B- and C-scans. They respectively generate the images of vertical and horizontal cross-sections of a test specimen. The data acquisition and construction for spectral B- and C scans are the same as described in Section 3.1. However, in spectral B-scan one only has to perform impact echo tests along a test line. Therefore, n_y=1 in B-scan.

For the purpose of imaging, the matrix $V[i,j,k]$ needs to be transformed into a matrix of color scales $c[i,j,k]$:

$$c[i,j,k] = \begin{cases} c_{\max} & V[i,j,k] > V_{\max} \\ c_{\max} \dfrac{V[i,j,k] - V_{\min}}{V_{\max} - V_{\min}} & V_{\min} < V[i,j,k] < V_{\max} \\ 0 & V[i,j,k] < V_{\min} \end{cases} \qquad (2)$$

where $c_{\max}$ is the upper bound of the color scale, and $[V_{\min}, V_{\max}]$ defines the range in which $V[i,j,k]$ is mapped linearly to $c[i,j,k]$. If $V[i,j,k]$ exceeds $V_{\max}$, the color scale is set to $c_{\max}$; if $V[i,j,k]$ is less than $V_{\min}$, the color scale is set to 0. Unless specified otherwise, $V_{\max}$ and $V_{\min}$ are chosen to be the maximum and minimum of the volume data, respectively. However, one can increase the value of $V_{\min}$ to suppress the noise and enhance the contrast of the image (Liu & Yeh, 2010). The contrast ratio $V_{\min}/V_{\max}$ that yields a satisfactory result can be obtained by adjusting the ratio manually.

In spectral B-scan, the image of the vertical section under the test line can be obtained simply by using $c[i, j = 1, k]$ to generate a 2D density plot. Notice that $c[i,j,k]$ reflects spectral amplitude. If a peak appears in the ith spectrum at frequency $k\Delta f$, the corresponding color scale is high and one can see a clear spot at location $x = i\Delta x$, $f = k\Delta f$ on the B-scan image. The clear spots will connect into a clear stripe if a crack exists. As such, one can detect the size and location of the crack in the concrete.

The spectral C-scan constructs an image for a horizontal section. Hence, one has to select the depth of the horizontal section to be examined. Suppose the depth corresponds to frequency $f = K\Delta f$, according to Eq. 1. The spectral C-scan image of the horizontal section can be obtained by using $c[i, j, k = K]$ to generate a 2D density plot.

Theoretically, the color of the image is homogeneous if no defect exists. If the section does contain a defect, there will be peaks in the spectra. Hence, one can determine if there is a defect simply by examining the color variation of the image.

In the following, numerical examples are given to illustrate the spectral B- and C-scan methods. Figure 3 shows the spectral B-scan images of the vertical sections under test line (a) x=16 cm and (b) x=40 cm. The crack occurs in the range $24 \le y \le 56$ cm. Hence, the first section contains no crack while the second section does. One can see that there are only horizontal stripes in Fig. 3(a). The stripe with the highest color scale (red) appears at f=10 kHz. Since the longitudinal wave velocity C_P=4000 m/s, this frequency corresponds to the depth of the bottom, 20 cm, according to Eq. 1. The bright stripe near 20 kHz is caused by the multiple peaks of the Fourier spectra. There are also red stripes at the bottom of the image. They are induced by the lower-mode vibrations of the specimen.

Figure 3(b) looks quite different from Fig 3(a). One can find an inclined red stripe occurring in the crack range. Outside that range, the image resumes the no-crack pattern, that is, red horizontal stripes appearing near f =10 kHz, denoting the bottom of the specimen. Although the B-scan image reveals the existence of the inclined crack, it does not exhibit the profile of the specimen under the test line. This is certainly because the vertical axis is frequency, not depth.

Figure 4 shows the spectral C-scan images of the horizontal sections at depth (a) 4 cm, (b) 10 cm and (c) 20 cm. Figure 4(a) looks just like a blue rectangle, implying that the cross-section contains no reflector. The image in Fig. 4(b) contains a red zone, depicting the crack on the cross-section. The yellow and cyan zones in the image both denote concrete, but the cyan zone is the concrete under the crack. Figure 4(c) shows the C-scan image at the bottom of the specimen. A cyan zone appears at the center of the image, surround by red zone. It can be considered as the shadow cast by the crack because the waves are blocked by the crack. The cyan zone is not a square because stress waves may go around the crack edge and reach the bottom when the test point is near the top of the edge. This zone provides a supplementary evidence for the existence of a defect above this region.
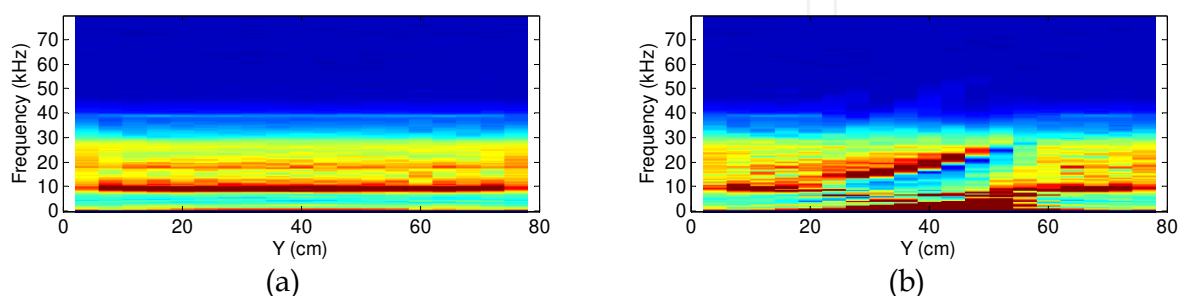
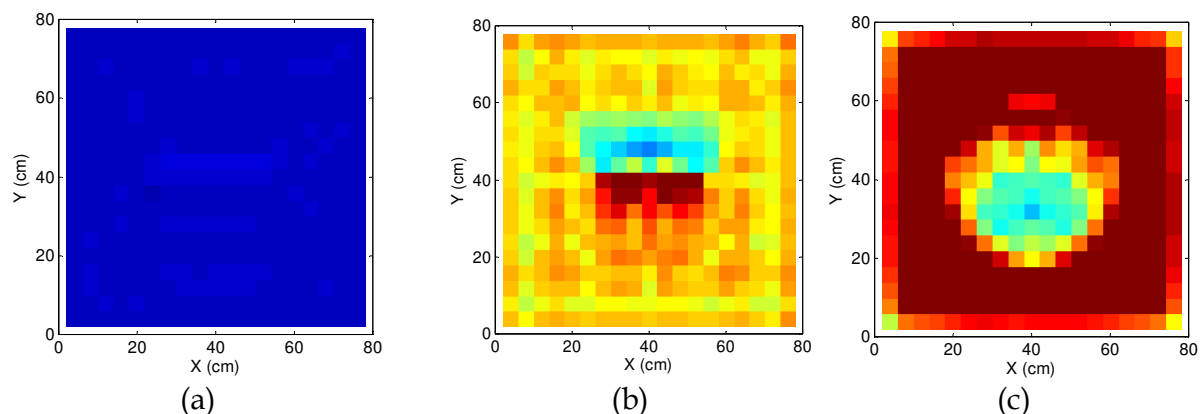Fig. 3. Spectral B-scan of cross-sections under test lines (a) x=16 cm and (b) x=40 cm

Fig. 4. Spectral C-scan of cross-sections at depth (a) 4 cm, (b) 10 cm, and (c) 20 cm

3.3 Spectral tomography

In the spectral B–scan method, the Fourier spectra of the test signals are assembled to construct an image of the test cross–section. Such image certainly provides useful information about internal defects. However, the vertical axis of the image is frequency. Hence, the spectral B-scan does not provide a "picture" of the test section.

In order to provide a more intuitive image, the vertical spectral tomography was proposed by Liu and Yeh (2010) . The imaging process of the vertical spectral tomography is the same as in spectral B-scan except that the Fourier spectra are replaced by depth spectra. Liu and Yeh (2011) extended the notion further to tomography of arbitrary cross–sections. As such, the inspector could examine the interior of a structure from various angles to get better understanding of its condition. The spectral C-scan is only a special case of spectral tomography.

In spectral tomography, the volume data is constructed using the depth spectra of the impact echo test. Similar to the spectral B- and C-scan, the matrix $V[i,j,k]$ is transformed into a matrix of color scales $c[i,j,k]$ according to Eq. 2. Then, the matrix $c[i,j,k]$ is used to produce tomograms for designated cross–sections.

Consider a cross–section defined by $\mathbf{n}^T\mathbf{x}+b=0$, where $\mathbf{n}$ is the outward normal of the cross–section, and $\mathbf{x}=[x,y,z]$ is the position vector. The spectral tomogram can be generated as follows:

1. Define a new coordinate system $\mathbf{x}'$ such that the $x'-y'$ plane coincides with the cross–section, as shown in Fig. 5(a). The coordinates in the new and old systems are related by

$$\mathbf{x}'=\mathbf{Q}^T(\mathbf{x}-\mathbf{t}) \tag{3}$$

where $\mathbf{Q}$ is the rotation matrix with component $Q(i,j)=\mathbf{e}_i\cdot\mathbf{e}'_j$, and $\mathbf{t}$ is the translation vector.

The coordinate transformation defined in Eq. (3) is not unique. $\mathbf{t}$ can be easily defined by choosing a point on the cross-section as the origin of the new coordinate system. $\mathbf{Q}$ can be constructed as follows. Suppose $\mathbf{n}=[p,\ q,\ r]^T$ is the outward normal of the cross–section, where $p^2+q^2+r^2=1$. The new base vectors can be selected as $\mathbf{e}'_z=\mathbf{n}$, $\mathbf{e}'_x=\mathbf{e}_z\times\mathbf{e}'_z$, and $\mathbf{e}'_y=\mathbf{e}'_z\times\mathbf{e}'_x$. Hence,

$$\mathbf{e}'_x=\frac{1}{\sqrt{1-r^2}}\begin{bmatrix}-q\\p\\0\end{bmatrix}\quad \mathbf{e}'_y=\frac{1}{\sqrt{1-r^2}}\begin{bmatrix}-pr\\-qr\\1-r^2\end{bmatrix}\quad \mathbf{e}'_z=\begin{bmatrix}p\\q\\r\end{bmatrix} \tag{4}$$

and

$$\mathbf{Q}=\begin{bmatrix}\dfrac{-q}{\sqrt{1-r^2}}&\dfrac{-pr}{\sqrt{1-r^2}}&p\\[3mm]\dfrac{p}{\sqrt{1-r^2}}&\dfrac{-qr}{\sqrt{1-r^2}}&q\\[3mm]0&\sqrt{1-r^2}&r\end{bmatrix} \tag{5}$$

2. Obtain the orthographic projection of the $L_x\times L_y\times L_z$ solid on the $x'-y'$ plane, and find a coordinate rectangle to enclose the projection, as shown in Fig. 5(b).

The orthographic projection of the solid can be obtained by projecting the vertices of the solid on the $x'-y'$ plane. The location of a projected vertex is simply the new coordinates (x',y') of that vertex obtained by Eq. (3). Suppose (x',y') satisfies $x'_{\min}\le x'\le x'_{\max}$ and $y'_{\min}\le y'\le y'_{\max}$ for every vertex. Then, the bounding rectangle is formed by the coordinate lines $x'=x'_{\min}$, $x'=x'_{\max}$, $y'=y'_{\min}$, and $y'=y'_{\max}$.

3.   Draw a mesh of square grids on the rectangle. For each grid, using Eq. (3) to transform the location of its center $\mathbf{x}'_c = \begin{bmatrix} x'_c, & y'_c, & 0 \end{bmatrix}$ back to the original coordinate system, i.e.,

$$\mathbf{x}_c = \mathbf{Q}\mathbf{x}'_c + \mathbf{t} \tag{6}$$

4.   Use $\mathbf{x}_c$ to determine in which voxel the center is located. Then, determine the color scale of the grid $c(\mathbf{x}_c)$ from the volume data. If $\mathbf{x}_c$ is outside the volume, no color scale is assigned and the pixel is transparent.

5.   Construct the tomogram of the cross–section by filling each grid with its color $c(\mathbf{x}_c)$.

Notice that in Step 3, each grid in the mesh corresponds to a pixel in the tomogram. It is advisable to adopt a fine mesh so that one can obtain a high-quality image. The resolution of the tomogram is certainly limited by the voxel size of the volume data. However, a pixel in the tomogram may pass through more than one voxel in the solid. A fine mesh helps to display the boundary between adjacent voxels more precisely. Furthermore, it helps to better delineate the borderline of the cross-section in the tomogram. Take the cross-section in Fig. 5 for example. The borderline of the cross-section is a hexagon. Since only pixels with its center located inside the volume are colored, the tomogram of the cross-section appears as the colored polygon in Fig. 5(b). It is seen that some segments of the borderline become zigzag. Apparently, the zigzag borderline approximates the true boundary better if a finer mesh is adopted.

The proposed spectral tomography does not provide the velocity profile of a test section as most conventional nondestructive techniques do. Instead, the spectral tomogram should be considered as a profile of reflection energy due to the impact.

In the following, a numerical example is presented to illustrate the spectral tomography. Figure 6 shows the horizontal tomograms constructed at depth (a) 20 cm, (b) 12 cm, and (c) 9 cm, respectively. Similar to Fig. 4, the crack casts a shadow on the bottom tomogram in Fig. 6(a). Bright stripes appear in Figs. 6(b) to (c), depicting the crack on each cross-section. Since this is a slant crack, the bright stripes shift along the y direction as the cross-section moves up. In this case, it is difficult to get an overall picture of the crack using horizontal tomograms alone.

Figure 7 shows the vertical tomograms along x= (a) 18 cm and (b) 40 cm, respectively. No crack presents on the first cross-section. Hence, one only finds bright stripes at the bottom of Fig. 7(a). In contrast, the slant crack is clearly depicted on the tomogram in Fig. 7(b). One can use this tomogram to determine the length and inclination of the crack.

It should be mentioned that the thickness of the bright stripe in Fig. 7(b) does not represent the thickness of the crack. In fact, the impact echo test cannot provide information about the thickness of the crack. The thickness of the bright stripe results from the width of the echo peak in the depth spectra. Hence, the true depth of the crack should be determined based on the location of the brightest pixels in the tomogram.

One may construct oblique tomograms to get a picture of the whole crack, as shown in Fig. 8. The slopes of the cross-sections vary from 0° to 90°. One can see that the area of the crack image is maximal when the slope is around 14°, coincident with the crack orientation. Hence, Fig. 8(c) provides the best picture of the crack among the tomograms. The crack

image is narrower near the shallow edge of the crack. Nevertheless, one can use the bright zone to estimate the size of the crack. This is quite difficult if only vertical or horizontal tomograms are available.
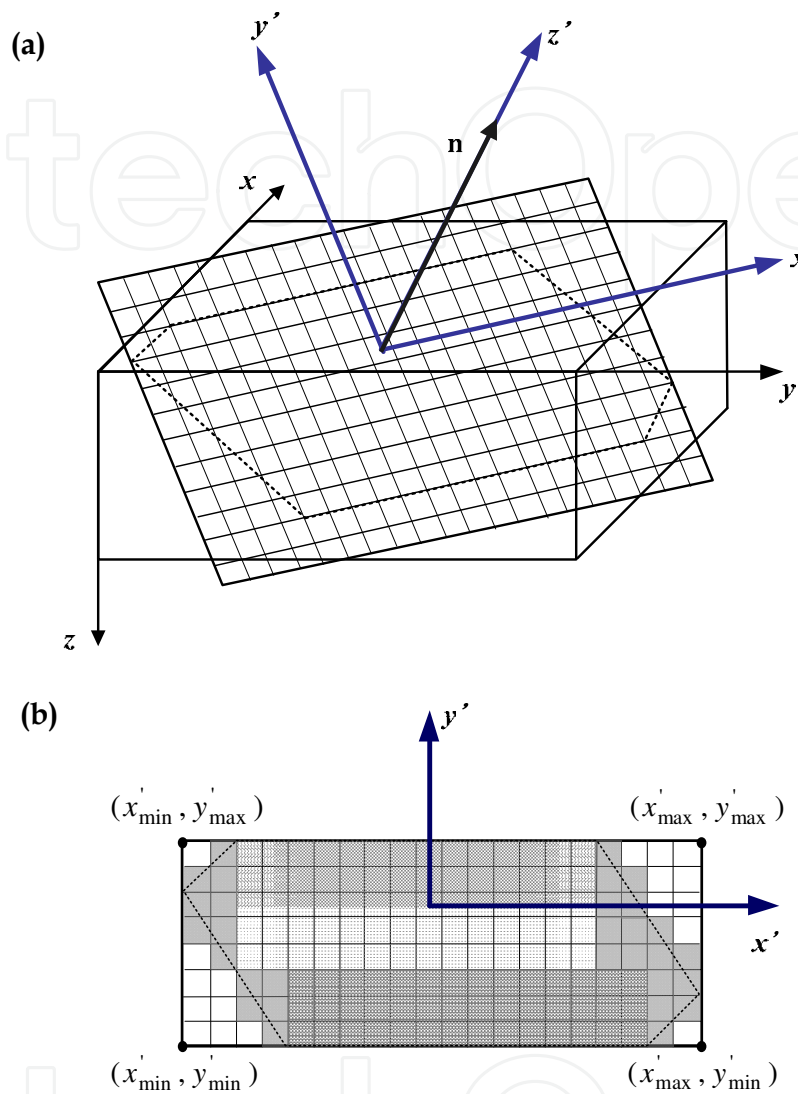

Fig. 5. (a) Coordinate transformation in tomography and (b) orthographic projection of specimen on the $x' - y'$ plane
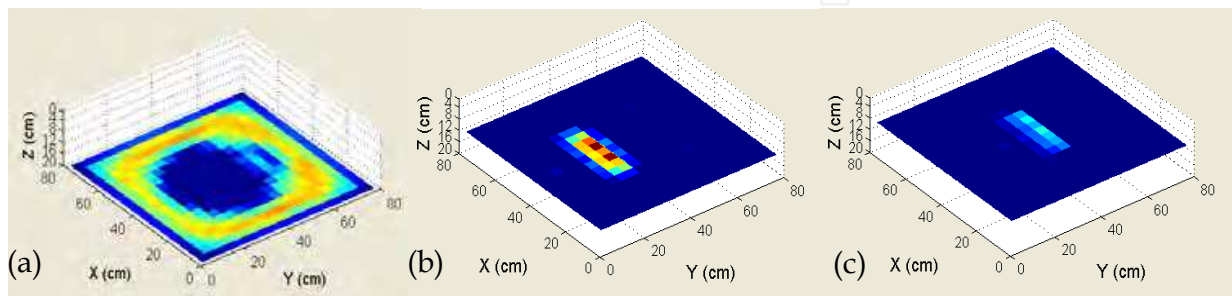

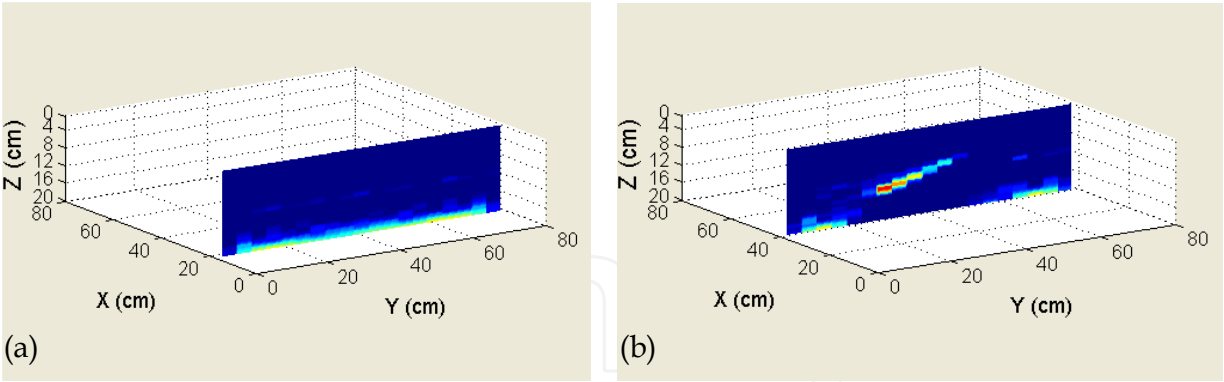Fig. 6. Horizontal tomograms at depth (a) 20 cm, (b) 12 cm and (b) 9 cm

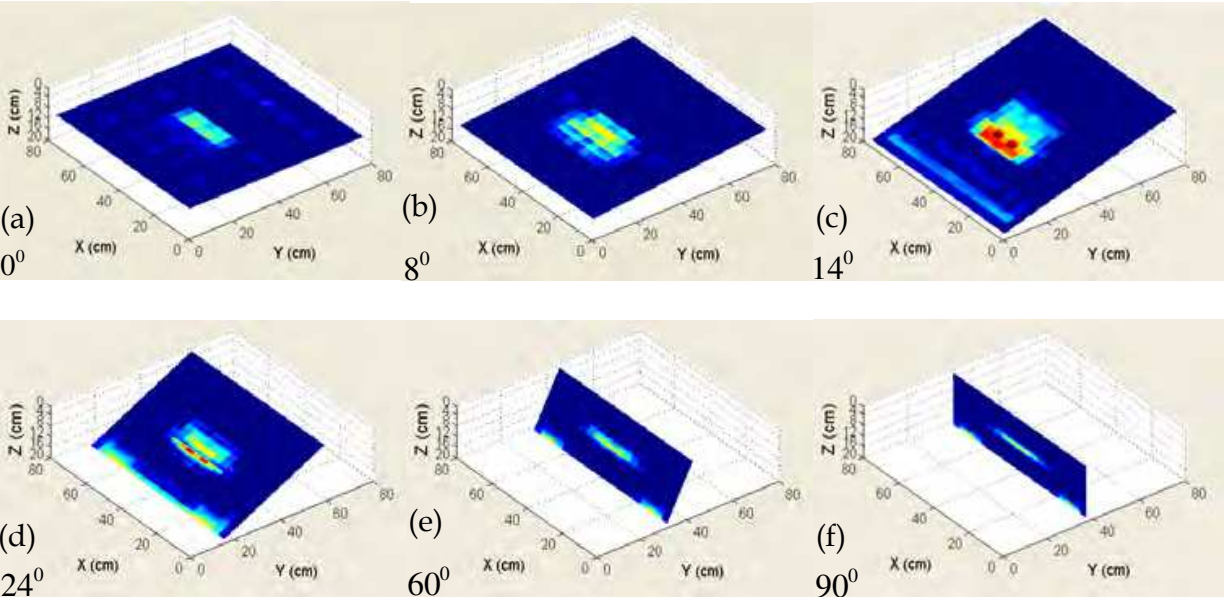Fig. 7. Vertical tomograms along x = (a) 18 cm and (b) 40 cm

Fig. 8. Oblique tomograms with slopes (a) 0°, (b) 8°, (c) 14°, (d) 24°, (e) 60°, and (f) 90°

This numerical example demonstrates that the inspector can use spectral tomography to examine any cross-section of a specimen. To get an overall assessment of the interior condition, it is advisable to examine the specimen in a systematic way rather than scan randomly. An inspection procedure is proposed herein: Firstly, construct a horizontal tomogram at the bottom of the specimen to find the defect zone. Then, construct a series of horizontal or vertical tomograms to find the location, size, shape, and orientation of the defect. Finally, based on the scanning results, perform oblique tomography to get a better image of the defect if necessary.

Figure 9 shows the results of spectral tomography in the model test. From Fig. 9(a), one can see the dark zone also forms beneath the crack. Figure 9(b) is the vertical tomogram along x=44 cm. The result is similar to that of numerical test. Bright zones occur at the crack and bottom. Despite noise, one can easily detect the inclination of the crack using this tomogram. Figure 9(c) shows the oblique tomogram of the crack plane. A bright zone appears in the crack area.
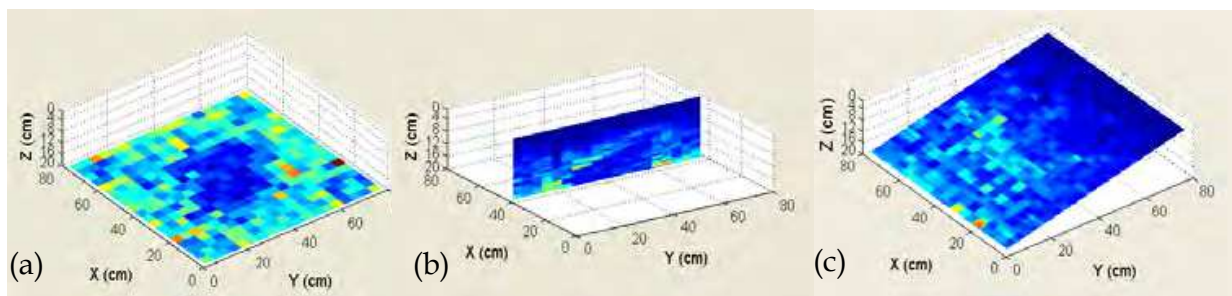
Fig. 9. Model test, (a) horizontal tomogram at the bottom, (b) vertical tomogram at x=44 cm, and (c) oblique tomogram.

Although the test data have been normalized by the amplitude of the surface wave, the tomograms still look mottled. The deterioration of tomogram quality may come from variation of impact force, random noise, measurement error, and non-uniform material of the model test. Therefore, it is advisable to compare the tomograms of different angle and sectioning before making judgment. Regardless of the noise, the bright and dark zones in these tomograms still reveal the location, orientation, and size of the crack.

3.4 Surface rendering

With the progress of computer graphics, 3D display becomes a trend in the processing of volume data. The methods that render 3D images are called volume visualization techniques. There are two branches techniques, namely, surface rendering and volume rendering. The surface rendering technique was proposed by Yeh and Liu (2009) to depict the internal cracks in concrete structures.

The surface rendering method is equivalent to drawing contour lines in a 2D density plot. Consider the vertical tomogram in Fig. 10(a) for example. If one selects an iso-value 104, one gets contour line 1; if one chooses a different iso-value 208, contour line 2 is obtained, as shown in Fig. 10(b). Apparently, if the iso-value is chosen properly, the contour line will depict the location of an interface. The same idea can be extended to the 3D case.
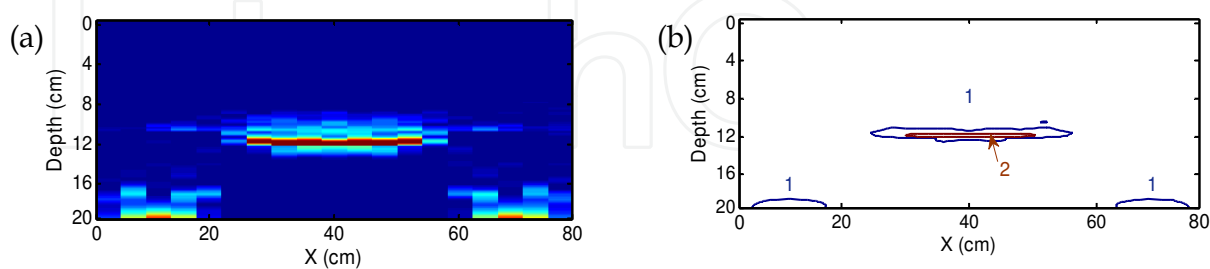

Fig. 10. 2D analogy of surface rendering (a) vertical tomogram and (b) contour plot

The main idea of surface rendering is to abstract the iso-surface from the volume data, i.e., to find a surface with the same spectral amplitude. Let $V(x,y,z)$ denote the volume data. The iso-surface corresponding to iso-value C can be represented as:

$$\{(x,y,d):V(x,y,d)=C\} \tag{7}$$

Once an iso-value is assigned, one can use triangular patches to generate an iso-surface. Similar to the contour lines in Fig. 10, if the iso-value is chosen properly, the iso-surface will depict the location of an interface in the specimen.

After the iso-surface is generated, it is projected to a 2D view plane. Notice that when a 3D object is projected to a 2D plane, a sphere will appear as a circle and a cube is turned into a hexagon. In order to obtain a stereograph, shading and lighting are necessary.

The Phong reflection model is a popular and effective approach for this end (Angel, 2006). This model assumes three types of light-material interactions, namely, ambient, diffuse, and specular reflection. The intensity of the reflected light is dependent on four vectors: the normal vector of the surface $\mathbf{N}$, the viewer vector $\mathbf{V}$, the light source vector $\mathbf{L}$, and the reflected ray vector $\mathbf{R}$.

The ambient light has the same intensity in the space. When it encounters a surface, it is absorbed and reflected. The intensity of the ambient reflection I_a is as follows:

$$I_a = K_a L_a \quad 0 \le K_a \le 1 \tag{8}$$

where K_a is the ambient reflection coefficient and L_a is the intensity of the ambient light.

The diffuse reflection is characterized by the roughness of the surface. The intensity of the reflected light depends on the material and incident direction of the light. Since each point on the surface has a different normal vector, it will reflect different amount of light. The intensity of the diffuse reflection I_d is as follows:

$$I_d = K_d L_d \mathbf{L} \cdot \mathbf{N} \quad 0 \le K_d \le 1 \tag{9}$$

where K_d is the diffuse reflection coefficient and L_d is the intensity of the incident diffuse light.

The specular reflection is used to highlight the shiny part of surface. Although the ambient and diffuse reflection make the image look three-dimensional, the lack of specular reflection would make the surface look dull. The intensity of the specular reflection is as follows:

$$I_s = K_s L_s (\mathbf{R} \cdot \mathbf{V})^\beta \quad 0 \le K_s \le 1, \ \beta \ge 1 \tag{10}$$

where K_s is the diffuse reflection coefficient, β is the shininess coefficient, and L_s is the intensity of incident specular light. Usually, $L_s = L_d$. As β increases, the reflected light tends to concentrate on a smaller region.

The total intensity of the reflected light from an object is the sum of I_a, I_d, and I_s. The coefficients K_a, K_d, K_s, and β are taken as 0.6, 0.8, 0.5, and 150, respectively, in the following examples.

Figure 11 shows the top, side, and oblique views of the surface rendering image of the numerical model. An iso-surface denoting the crack is observed in all three images at the correct location. One can also find the bottom of the specimen in the image. However, a hole is formed in the bottom beneath the crack, as shown in Fig. 11(a). This is because the waves are blocked by the crack and cannot reach the bottom.

From the side view in Fig. 11(b), one can see that the crack is thicker than the real crack. Actually, the impact echo test cannot provide thickness of the crack. The thickness of crack in the image results from the width of echo peak in the spectra. Therefore, the true depth of the crack is around the center of the iso-surface.
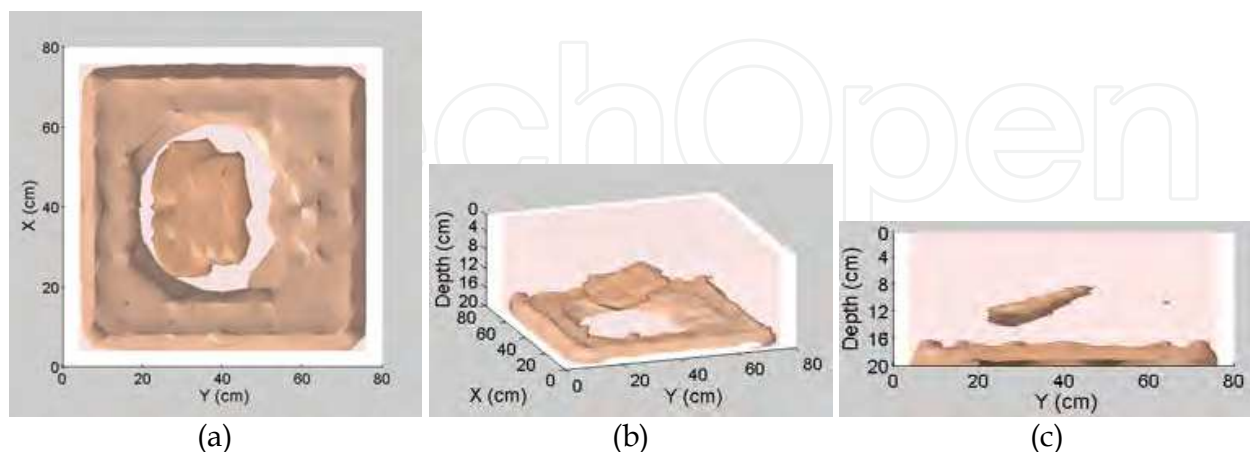

(a)   (b)   (c)

Fig. 11. Surface rendering of numerical model, (a) top view, (b) side view, and (c) oblique view

In practical applications, it is critical to choose a proper iso-value because different iso-values result in different images. The iso-value of the images in Fig. 11 is 15. Figure 12 shows a series of surface rendering images with iso-values 12, 18, and 22, respectively. Clearly, the crack iso-surface shrinks as the iso-value increases. If the iso-value is too low, the iso-surface denoting the crack becomes a large layer. On the other hand, if the iso-value is too high, the crack iso-surface becomes excessively small. Since the hole can be considered as the "shadow" of the crack, the iso-value should be chosen such that the sizes of the crack and the hole match.

The surface rendering images of the experimental model are shown in Fig. 13. Because the experimental signals are contaminated by noise, the 3D images are not as clear as in the numerical example. The crack is not enveloped in a single iso-surface. Several iso-surfaces appear around the crack location instead. This is mainly because the impact source is unsteady. Normalization of the signals may reduce the influence of the intensity of the source function, but not the shape. Therefore, it is hard to find an appropriate iso-value to surround the crack by a single iso-surface.

Nevertheless, one can still manage to find the crack by viewing the specimen at different angles. For example, the side view in Fig. 13(b) provides a clear picture of the inclined crack. Furthermore, the hole beneath the crack is still visible in Figs. 13(a) and (c).

3.5 Volume rendering

The volume rendering technique was proposed by Yeh and Liu (2008) to construct 3D images based on impact echo data. The data acquisition and construction procedures are the same as described in Section 3.1.
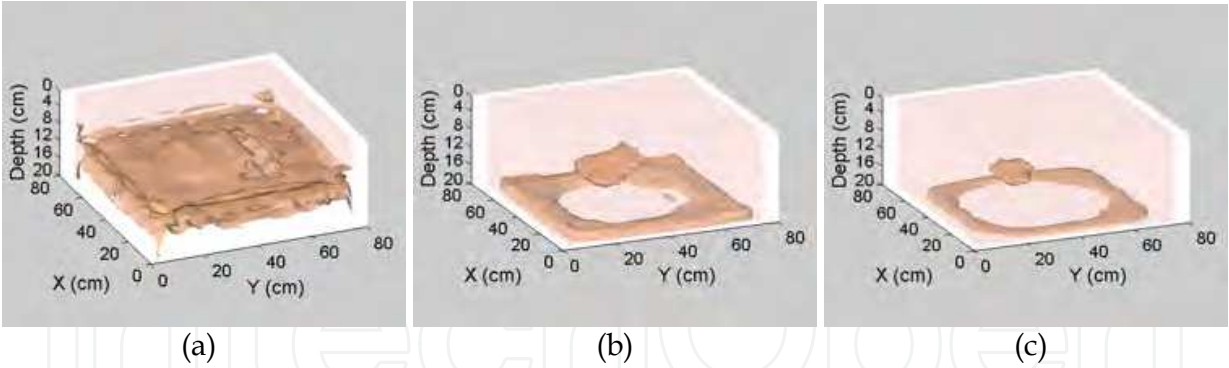
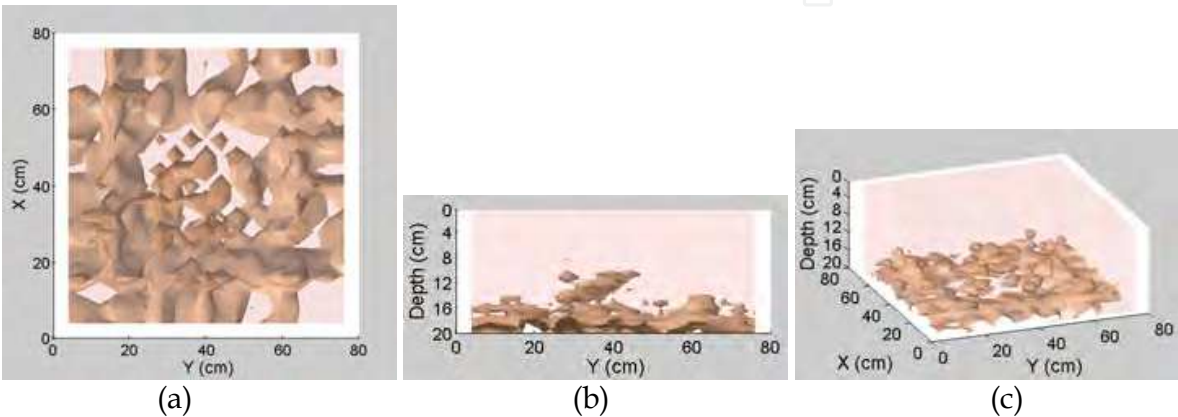Fig. 12. Surface rendering of the numerical model with iso-values (a) 12, (b) 18, and (c) 22

Fig. 13. Surface rendering of the experimental model, (a) top view, (b) side view, and (c) oblique view

In the volume rendering method, each voxel is assigned an opacity α based on the volume data such that $0 \le \alpha \le 1$. The opacity represents the level of difficulty that light goes through a voxel. If a voxel is complete opaque, $\alpha = 1$, and if it is complete transparent, $\alpha = 0$. The opacity of a voxel can be determined as follows:

$$\alpha[i,j,k] = \begin{cases} 1 & V > V_{max} \\ \dfrac{V[i,j,k] - V_{min}}{V_{max} - V_{min}} & V_{min} < V < V_{max} \\ 0 & V < V_{min} \end{cases} \tag{11}$$

As in spectral tomography, the default values of V_{max} and V_{min} are the maximum and minimum of the volume data, respectively.

The process of volume rendering is analogous to X-ray examination. To construct the volume rendering image, let parallel rays emitted from a light source behind the volume transmit through the volume and reach a projection plane, as shown in Fig. 14(a). When a ray passes through the volume, it accumulates the opacity of the voxels it encounters, as shown in Fig. 14(b). The compositing operation is a recursion of opacity, as shown in the following (Angel, 2006):

$$\alpha_{out} = (1 - \alpha)\alpha_{in} + \alpha \tag{12}$$

where α is the opacity of the current voxel, α_{in} is the accumulated opacity entering the voxel, and α_{out} is the accumulated opacity leaving the voxel. If $\alpha = 1$, then $\alpha_{out} = 1$ and the light is totally obstructed. On the other hand, if $\alpha = 0$, then $\alpha_{out} = \alpha_{in}$ and the light remains unchanged. Therefore, α is an indicator of the degree that light penetrates the voxel.

Equation 12 is applied recursively to determine the accumulated opacity of a ray until it leaves the volume and reaches the projection plane. After the accumulated opacity is obtained for each ray penetrating the volume, one can draw a density plot of the accumulated opacity on the projection plane. This method is called the ray casting (Watt, 2000). Although the ray casting method describes the concept of imaging clearly, it is time-consuming. Hence, the texture mapping technique has been proposed to speed up the imaging process (Engel et al., 2006).

Recall that in the impact echo test, an interface will induce a peak in the spectrum. Hence, if a defect appears in the volume, the spectral amplitude along the defect is large, so is the opacity. Apparently, the rays that pass through the defect will be dimmer than the rays that do not. Hence, one will find a shadow in the image if there is a defect in the volume.
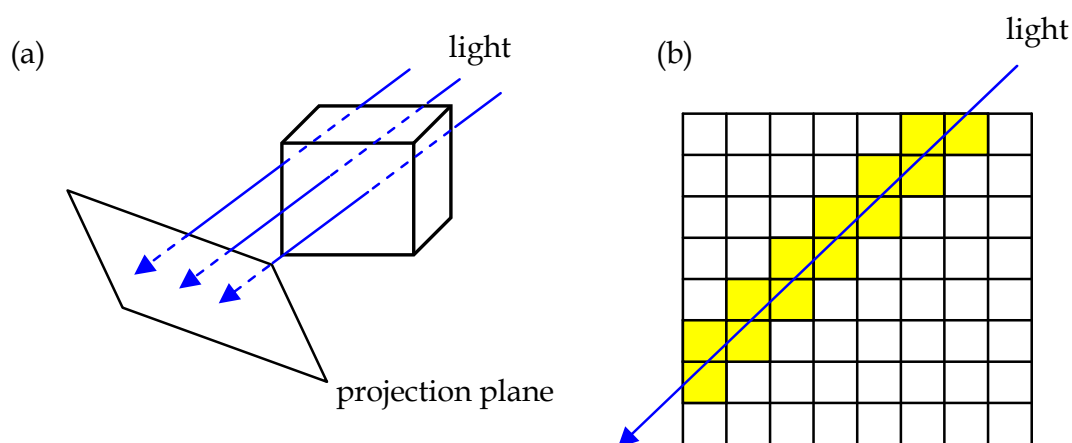
Fig. 14. The volume rendering method

The signals obtained in the impact echo tests inevitably contain noise. That may downgrade the quality of image and make the diagnosis difficult. This problem can be tackled by adjusting the relation between the volume data and the opacity, as defined in Eq. 11. It does not help to alter the value of $V_{\max}$. Hence, one can simply use its default value. The value of $V_{\min}$ can be increased to suppress noise and enhance the contrast of image.

Figure 15 shows the influence of $V_{\min}/V_{\max}$ on the volume rendering image. Generally speaking, as $V_{\min}/V_{\max}$ increases, the crack image gets clearer and the hole at the bottom gets larger. With $V_{\min}/V_{\max}$ below 20%, the image looks blurry, as seen in Figs. 15(a) and (b). When $V_{\min}/V_{\max}$ is increased to 30%, the crack and the hole at the bottom become visible. When $V_{\min}/V_{\max} = 40\%$, one gets a very good image of the specimen.

However, the contrast ratio should not be over raised. As $V_{\min}/V_{\max}$ reaches 50%, the crack starts to shrink and the size of the hole exceeds that of the crack. The situation is even worse as $V_{\min}/V_{\max} = 60\%$.

Notice that the optimal value of V_{min}/V_{max} may change from case to case. The inspector has to try different value to see which value yields the best result.
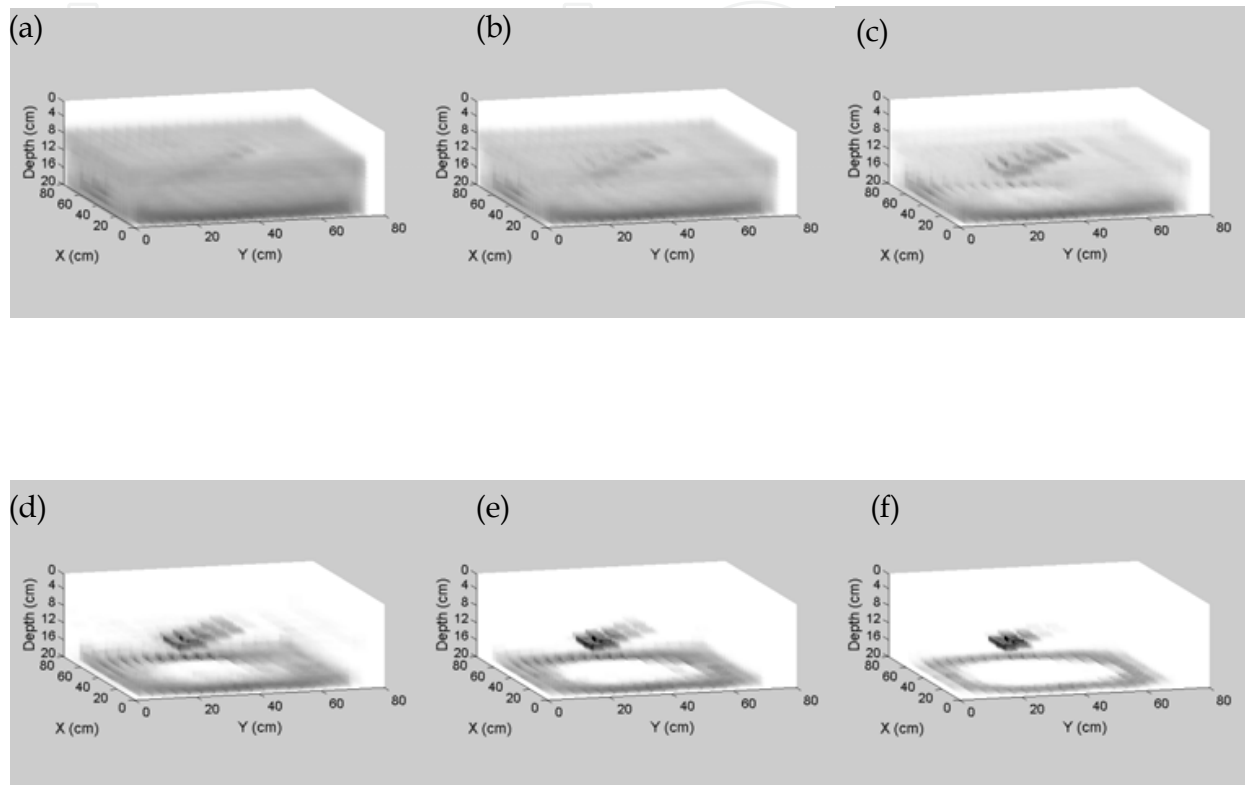

Fig. 15. Volume rendering of numerical model using V_{min}/V_{max} = (a) 10 %, (b) 20 %, (c) 30 %, (d) 40 %, (e) 50 %, (f) 60 %

Figure 16 show the volume rendering images of the experimental model with various view angles. The contrast of image is V_{min}/V_{max} =30%. The test data contain a lot of noise. Hence, the crack appears as a cluster of dark patches in the image.

In Fig. 16(a), one can find a cluster of dark patches in the central area of the image, denoting the crack. As one rotates the model, the hole at the bottom becomes visible, indicating the existence of a defect. The side view in Fig. 16(d) provides a clear view of the crack. The size and location of the crack can be estimated based on this image.

Although these images are not as clear as in the numerical examples, one can still locate the crack by viewing the specimen from different angles. This is best done with an interactive imaging program that allows the inspector to interactively adjust the view angle and the contrast ratio. With the aid of such program, one can easily manipulate the image. Furthermore, as one adjusts the view angle gradually, the image becomes stereoscopic. That helps the inspector to interpret the image. Unfortunately, such effect cannot be demonstrated in this book.
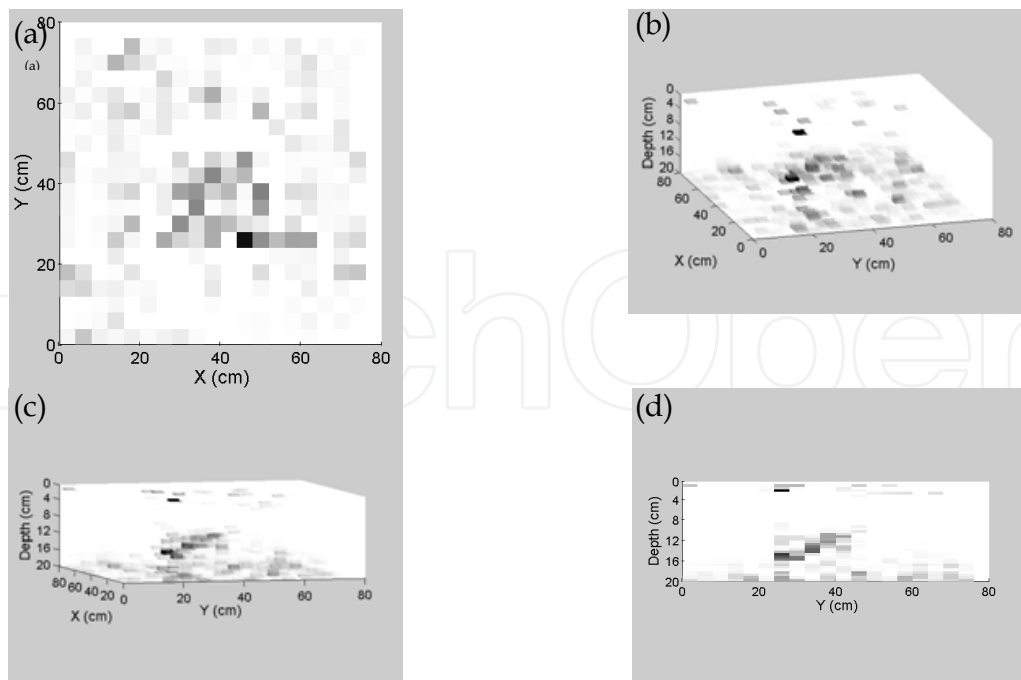
Fig. 16. Volume rendering of experimental model test with various view angles

4. Conclusion

This chapter introduces several methods to construct the image of concrete interior using impact echo data, including the spectral B-scan, spectral C-scan, spectral tomography, surface rendering, and volume rendering. With these imaging methods, the inspector may examine the interior of a structure to get better understanding of its health condition.

The imaging procedure contains three steps: data acquisition, data construction, and image rendering. Basically, the first two steps are the same for all the imaging methods. Firstly, a series of impact echo tests are performed at the grids of a mesh on the surface of the concrete. Then, the time signals are transformed into frequency spectra or depth spectra. Assembling the spectra into a 3D matrix yields the volume data, which could be used to construct images.

The spectral B- and C-scan are derived from ultrasonic scan. The spectral B-scan constructs a 2D density plot of the spectral amplitude on the vertical section under a test line; while the spectral C-scan constructs the plot for a horizontal section. Because the vertical axis of the spectral B-scan is frequency, it does not provide the profile of a vertical section. One may judge whether there is an internal defect by examining the discontinuity of horizontal stripes in B-scan. However, the size and location of the defect cannot be determined from the image directly.

The spectral C-scan, on the other hand, provides the profile of a horizontal section. Thus, one can use the image to determine the size and location of an internal defect. However, it is sometimes difficult to get an overall picture of the concrete interior by viewing horizontal sections alone.

The spectral tomogram can be considered as an extension of the spectral C-scan. It can be used to construct the profile image for arbitrary cross–sections. The inspector can observe the interior of a structure from different angles and by different sectioning. As such, the

internal defects in concrete structures can be easily located. Through the numerical and experimental examples, it is seen that the spectral tomography can depict the internal crack of the concrete specimen successfully. When a crack exists in the concrete, it appears as a bright zone in the tomogram. Furthermore, no bright stripes appear beneath the crack at the bottom of the tomogram because the waves are blocked by the crack. This provides supplementary information about the size and location of the crack.

Surface rendering and volume rendering are 3D imaging techniques. The idea of surface rendering is to abstract the iso-surface from the volume data. In surface rendering, a defect is represented by one or several iso-surfaces, which can be used to estimate its size and location. Same as in spectral tomogram, a hole, approximate the size of defect, appears at the bottom beneath the defect.

Volume rendering is analogous to X-ray examination: Parallel rays are generated, transmit through a specimen, and reach a projection plane. If a defect exists in the specimen, the voxels covering the defect would have high opacity. Hence, a dark zone forms in the volume rendering image. If the view angle is chosen properly, one could also find a hole at the bottom beneath the defect.

Comparing these methods, one can see that each method has its own strength and weakness. Volume rendering is a robust technique; it is not sensitive to the interferences in spectra. Surface rendering is sensitive to noise, but it can depict the details of a defect. Spectral tomography is robust and insensitive to noise. However, it does not provide a 3D image and one can only view the specimen by sectioning.

To maintain good balance between robustness and precision, the inspector should take advantage of the strength of each method. One may apply volume rendering to get an overall picture of the specimen and to find the approximate location of the defect, if any. Then, use surface rendering or spectral tomography to observe the details.

It is seen in the experimental examples that the presence of noise downgrades the quality of images, no matter which method is adopted. Unfortunately, the test data is always noisy and the impact source is unsteady in real applications. The images obtained are sometimes difficult to interpret. In that situation, an interactive imaging program is indispensable. With the interactive graphic interface, one can adjust the imaging parameters or view angle arbitrarily and get an updated image instantly. As such, one may attain a better view of the specimen easily. More importantly, the 3D image appears stereoscopic as one changes the view angle gradually. Therefore, one can tell which object is in the front and which is in the back. This is useful especially when the quality of the image is poor.

The imaging methods presented in this chapter may provide the most direct information about the defects in concrete structures. However, its practical applications are hindered by two issues. Firstly, it is very time-consuming because a vast amount of tests need to be conducted. Secondly, the unsteadiness of the impact source deteriorates the quality of the image. It seems that an automatic test system is the solution to these problems. It is hope that such system can be developed in the near future so that the imaging techniques can be widely applied in the inspection of concrete structures.

5. Acknowledgment

6. References

Abraham, O., Leonard, C., Cote, P. & Piwakowski, B. (2000). Time-frequency Analysis of Impact-Echo Signals: Numerical Modeling and Experimental Validation. ACI Materials Journal, Vol.97, No.6, pp. 645-657

Angel, E. (2006). Interactive Computer graphics: a top-down approach using OpenGL 4th Ed., Addison Wesley, ISBN 0-321-3125-2X, MA

Engel, K., Hadwiger, M., Kniss, J. M., Rezk-Salama, C. & Weiskopf, D. (2006). Real-Time Volume Graphics, A K Peter, Ltd., ISBN 1-56881-266-3, Wellesley, MA

Gibson, A. & Popovics, J. S. (2005). Lamb wave basis for impact-echo method analysis. ASCE Journal of Engineering Mechanics, Vol.131, No.4, pp. 438-443

Goldsmith, W. (1960). Impact：The Theory and Physical Behavior of Colliding Solids, Edward Arnold Ltd., London

Hallquist, J. O. (2003). LS-DYNA Keyword User's Manual, Livermore Software Technology Corporation, Livermore

Kohl, C., Krause, M., Maierhofer, C. & Wostmann, J. (2005). 2D- and 3D-visualisation of NDT-data using data fusion technique. Materials and Structures, Vol.38, No.9, pp. 817-826

Lin, C. C., Liu, P. L. & Yeh, P. L. (2009). Application of empirical mode decomposition in the impact-echo test. NDT & E International, Vol.42, No.7, pp. 589~588

Lin, Y. & Sansalone, M. (1992). Transient Response of Thick Circular and Square Bars Subjected to Transverse Elastic Impact. J. Acoustical Society of America, Vol.91, No.2, pp. 885-893

Liu, P. L. & Yeh, P. L. (2008). Imaging of internal cracks in concrete structures using the volume rendering technique, 17th WCNDT, Shanghai, China, Oct. 25-28, 2008

Liu, P. L. & Yeh, P. L. (2010). Vertical Spectral Tomography of Concrete Structures Based on Impact Echo Depth Spectra. NDT & E International, Vol.43, No.1, pp. 45-53

Liu, P. L. & Yiu, C. Y. (2002). Imaging Of Concrete Defects Using Elastic Wave Tests, Proceedings, the 2002 Far-East Conference on Nondestructive Testing, Tokyo, Japan, Oct. 21-24, 2002

Liu, P.-L. & Yeh, P.-L. (2011). Spectral Tomography of Concrete Structures Based on Impact Echo Depth Spectra. NDT & E International, Vol.44, No.8, pp. 692~702

Sansalone, M. & Carino, N. J. (1986). Impact-Echo: A Method for Flaw Detection in Concrete Using Transient Stress Waves, Gaithersburg, MD: National Bureau of Standard

Sansalone, M. J. & Streett, W. B. (1997). Impact-echo: nondestructive evaluation of concrete and masonry, Bullbrier Press, Ithaca, N.Y.

Schubert, F. & Köhler, B. (2008). Ten Lectures on Impact-Echo. Journal of Nondestructive Evaluation, Vol.27, pp. 5-21

Schubert, F., Wiggenhauser, H. & Lausch, R. (2004). On the Accuracy of Thickness Measurements in Impact-echo Testing of Finite Concrete Specimens-numerical and Experimental Results. Ultrasonics, Vol.42, pp. 897-901

Watt, A. (2000). 3D Computer Graphics, Addison Wesley, ISBN 0-201-39855-9, Edinburgh Gate, British

Yeh, P. L. & Liu, P. L. (2008). Application of the Wavelet Transform and the Enhanced Fourier Spectrum in the Impact Echo Test. NDT & E International, Vol.41, No.5, pp. 382-394

Yeh, P. L. & Liu, P. L. (2009). Imaging of internal cracks in concrete structures using the surface rendering technique. NDT & E International, Vol.42, No.3, pp. 181-187

Zhu, J. Y. & Popovics, J. S. (2007). Imaging concrete structures using air-coupled impact-echo. ASCE Journal of Engineering Mechanics, Vol.133, No.6, pp. 628-640
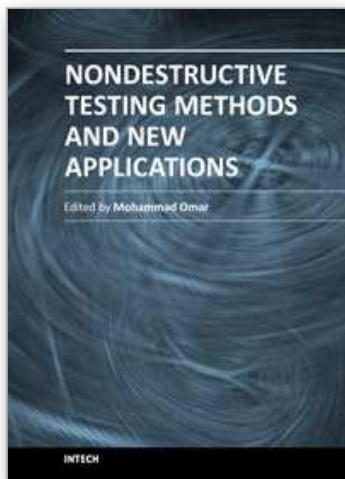
Nondestructive Testing Methods and New Applications

Edited by Dr. Mohammad Omar

Nondestructive testing enables scientists and engineers to evaluate the integrity of their structures and the properties of their materials or components non-intrusively, and in some instances in real-time fashion. Applying the Nondestructive techniques and modalities offers valuable savings and guarantees the quality of engineered systems and products. This technology can be employed through different modalities that include contact methods such as ultrasonic, eddy current, magnetic particles, and liquid penetrant, in addition to contact-less methods such as in thermography, radiography, and shearography. This book seeks to introduce some of the Nondestructive testing methods from its theoretical fundamentals to its specific applications. Additionally, the text contains several novel implementations of such techniques in different fields, including the assessment of civil structures (concrete) to its application in medicine.

How to reference

In order to correctly reference this scholarly work, feel free to copy and paste the following:

Pei-Ling Liu and Po-Liang Yeh (2012). Imaging Methods of Concrete Structure Based on Impact-Echo Test, Nondestructive Testing Methods and New Applications, Dr. Mohammad Omar (Ed.), ISBN: 978-953-51-0108-6, InTech, Available from: http://www.intechopen.com/books/nondestructive-testing-methods-and-new-applications/imaging-methods-of-concrete-structure-based-on-impact-echo-test

INTECH
open science | open minds